INTERNATIONAL JOURNAL FOR NUMERICAL METHODS IN FLUIDS
Int. J. Numer. Meth. Fluids 2010; **62**:1–23
Published online 16 February 2009 in Wiley InterScience (www.interscience.wiley.com). DOI: 10.1002/fld.2006

Fluid–solid interaction problems with thermal convection using the immersed element-free Galerkin method

Claudio M. Pita[1] and Sergio D. Felicelli[1, 2, *, †]

[1]*Department of Mechanical Engineering, Mississippi State University, MS 39762, U.S.A.*
[2]*Center for Advanced Vehicular Systems, Mississippi State University, MS 39762, U.S.A.*

SUMMARY

In this work, the immersed element-free Galerkin method (IEFGM) is proposed for the solution of fluid–structure interaction (FSI) problems. In this technique, the FSI is represented as a volumetric force in the momentum equations. In IEFGM, a Lagrangian solid domain moves on top of an Eulerian fluid domain that spans over the entire computational region. The fluid domain is modeled using the finite element method and the solid domain is modeled using the element-free Galerkin method. The continuity between the solid and fluid domains is satisfied by means of a local approximation, in the vicinity of the solid domain, of the velocity field and the FSI force. Such an approximation is achieved using the moving least-squares technique. The method was applied to simulate the motion of a deformable disk moving in a viscous fluid due to the action of the gravitational force and the thermal convection of the fluid. An analysis of the main factors affecting the shape and trajectory of the solid body is presented. The method shows a distinct advantage for simulating FSI problems with highly deformable solids. Copyright © 2009 John Wiley & Sons, Ltd.

Received 29 September 2008; Revised 16 December 2008; Accepted 7 January 2009

KEY WORDS: fluid–structure interaction; meshfree methods; immersed element-free Galerkin method; thermal convection; moving least squares; adaptive re-meshing

1. INTRODUCTION

Numerical investigations involving large deformation-type problems require reliable numerical modeling and simulation techniques. According to Li and Liu [1], the finite element method (FEM) subdivision procedure is not always advantageous in computations involving large deformations.

*Correspondence to: Sergio D. Felicelli, Center for Advanced Vehicular Systems, Mississippi State University, MS 39762, U.S.A.
†E-mail: felicelli@me.msstate.edu

Contract/grant sponsor: National Science Foundation; contract/grant number: CTS-0553570
Contract/grant sponsor: Center for Advanced Vehicular Systems (CAVS)

For more than 30 years, many research efforts have been devoted to adapt the FEM subdivision to topological and geometrical changes in the domain of interest, occurring, for instance, during the deformation of the material. The so-called arbitrary Lagrangian Eulerian method is a finite element formulation that moves the mesh independently from the material motion, allowing mesh distortion to be minimized. But even this technique has its limitations for some practical problems involving large strain continuum deformation.

With the aim of finding a better approximation of continuum compatibility, a series of new discretization methods, called meshfree particle methods, were developed, Li and Liu [1], Belytschko *et al.* [2], and Liu [3]. Meshfree particle methods have been designed to improve the inadequacy of FEM discretization. The main idea of these innovative methods is to discretize a continuum by only a set of nodal points without additional mesh constraints. The meshfree methods have a clear advantage over the traditional FEMs because meshfree interpolants have a larger support size than FEM interpolants. In 1977, Gingold and Monaghan [4] and Lucy [5] initially developed the smoothed particle hydrodynamics (SPH) method for the simulation of astrophysics problems. Their breakthrough was a method for the calculation of derivatives that did not require a structured computational mesh. Review papers by Benz [6] and Monaghan [7] cover the early development of SPH. Libersky and Petchek [8] extended SPH to work with the full stress tensor in two dimensions. This addition allowed SPH to be used in problems where material strength is important. The development of SPH with strength of materials continued with extension to three dimensions by Libersky *et al.* [9], and the linking of SPH with existing finite element codes by Attaway *et al.* [10] and Johnson [11]. The introduction of material strength highlighted shortcomings in the basic method: accuracy, tensile instability, zero energy modes, and artificial viscosity. These shortcomings were identified in the first comprehensive analysis of the SPH method by Swegle *et al.* [12] and Wen *et al.* [13]. The problems of consistency and accuracy of the SPH method, identified by Belytschko *et al.* [14], were addressed by Randles and Libersky [15] and Vignjevic *et al.* [16]. This resulted in a normalized first-order consistent version of the SPH method with improved accuracy. The attempts to ensure first-order consistency in SPH led to the development of a number of variants of the SPH method, such as element-free Galerkin method (EFGM) by Belytschko *et al.* [2] and Krongauz and Belytschko [17], reproducing kernel particle method (RKPM) by Liu *et al.* [18, 19], moving least-squares (MLS) particle hydrodynamics by Dilts [20], and the meshless local Petrov Galerkin method by Atluri and Zhu [21]. These methods allow the restoration of consistency of any order by means of a correction function. It has been shown in [21] that the approximations based on corrected kernels, like RKPM, are equivalent to moving least-square approximations, like EFGM. The issue of stability was dealt with in the context of particle methods in general by Belytschko and Xiao [22], and independently by Randles *et al.* [23]. They reached the same conclusions as Swegle *et al.* [12] in his initial study.

The RKPM approximation functions have been used by Zhang and Gay [24] and Zhang *et al.* [25] to develop the immersed finite element method (IFEM) to model fluid–structure interaction (FSI) processes. In this method, a Lagrangian solid mesh moves on top of a background Eulerian fluid mesh that spans over the entire computational domain. The FSI is represented as a body force term in the momentum equations. Although the IFEM uses the mesh-free RKPM interpolants to couple the solid and fluid domains, a finite element discretization is used for both regions. An improvement of the IFEM with respect to the previously developed immersed boundary method is that the structural models in IFEM are not restricted to one-dimensional volumeless structures such as fibers; instead, they may occupy a finite volume in the fluid and a constitutive model can be used to calculate the deformation and stress in the solid.

DOI: 10.1002/fld

The immersed element-free Galerkin method (IEFGM) was recently introduced by Pita and Felicelli [26]. This technique combines aspects of the IFEM, developed by Zhang *et al.* [25], and the EFG method of Belytschko *et al.* [2]. In IEFGM, a Lagrangian solid domain moves on top of an Eulerian fluid domain that spans over the entire computational region. The fluid domain is modeled using the FEM, whereas the solid domain is modeled using the EFGM. The continuity between the solid and fluid regions is satisfied by means of a local approximation, in the vicinity of the solid domain, of the velocity field and the FSI force. Such an approximation is achieved using the MLS technique [27]. The innovative fluid–structure coupling of the IEFGM, based on the meshfree method and the MLS shape functions, allows the efficient handling of highly distorted solids, which would be quite difficult to achieve with adaptive finite element techniques.

The aim of this work is to show the capabilities of the IEFGM to handle FSI problems where the solid body undergoes large deformations. Several numerical examples are presented in which an elastic solid disk, with different values of density and the Young modulus, was submerged in a viscous Newtonian fluid under unsteady thermal convection. The trajectory and deformation of the solid were analyzed in each case to provide insight into the physics behind the fluid–structure interaction.

2. FORMULATION OF THE IEFGM

2.1. Basic definitions

Let us consider a two-dimensional deformable solid body, Ω^{s}, that is completely immersed in a fluid domain, Ω^{f}. These two domains do not intersect, and their union defines the computational domain Ω. Therefore we can write

$$\begin{aligned} \Omega^{\mathrm{f}} \cup \Omega^{\mathrm{s}} &= \Omega \\ \Omega^{\mathrm{f}} \cup \Omega^{\mathrm{s}} &= \Phi \end{aligned} \tag{1}$$

Assuming incompressible solid and fluid domains, and a no-slip condition between them, the union of the two domains can be treated as one continuum incompressible region with continuous velocity, pressure, and temperature fields. In this work, the fluid domain is modeled using the FEM with an Eulerian formulation where the independent variables are the node's time-invariant actual position $\mathbf{x}$ and the actual time t and the dependent variables are the velocity $\mathbf{v}$, the pressure p, and the temperature T. On the other hand, the solid domain is modeled using the EFGM with an updated Lagrangian formulation in which the independent variables are the particle's current position $\mathbf{x}^{\mathrm{s}}$ and the actual time t and the dependent variable is the particle's displacement $\mathbf{u}^{\mathrm{s}}$ defined as the difference between the current and previous position. A schematic of the fluid and solid domains including the independent variables of each formulation and the displacement of the solid particles is presented in Figure 1. Note that for clarity we use the notion of node to refer to the fluid domain (described with an FEM) and the notion of particle to make reference to the solid domain (described with an element-free method).

2.2. Overlapping domain

When the solid is completely immersed in the fluid, the real geometrical relationships between the solid and fluid domains are given by Equation (1). Following the approach adopted by

DOI: 10.1002/fld

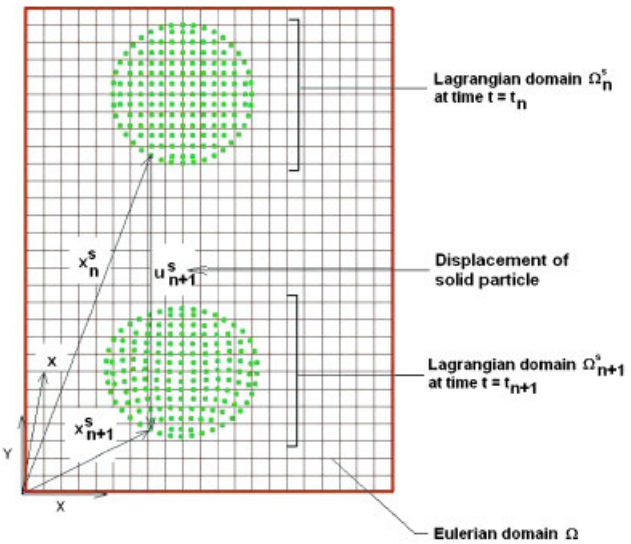

Figure 1. Definition of the solid (Lagrangian) domain and the fluid (Eulerian) domain. The Eulerian configuration is characterized by the time invariant position vector $\mathbf{x}$ whereas the Lagrangian configuration is characterized by the current position vector $\mathbf{x}^s$.

Zhang *et al.* [25] in their IFEM method, we assume that the fluid occupies the entire computational domain and that the solid region is placed on top of the fluid domain. This assumption introduces what is called an overlapping domain ($\bar{\Omega}$), which is the region where the solid and fluid domains coexist (i.e. $\bar{\Omega}=\Omega^s$). Note that this is a simplifying assumption and does not correspond with the real physical problem. This assumption simplifies the computations allowing the equations for the fluid and the solid domains to be solved independently. It also allows the independent discretization of the fluid and solid regions. The drawback of this simplification is that the overlapping domain introduces non-physical effects in the equations of motion that must be considered.

2.3. Governing equations

2.3.1. Solid domain. The FSI force within the solid domain Ω^s is denoted as $f_i^{\mathrm{FSI,s}}$, where FSI stands for fluid–structure interaction, s means that the expression is valid within the solid domain, and the sub-index i represents the ith Cartesian component of the force vector field. As in Li and Liu [1], Zhang and Gay [24], and Zhang *et al.* [25], this force can be written as

$$F_i^{\mathrm{FSI,s}} \stackrel{\mathrm{def}}{=} -(\rho^s-\rho^f)\frac{\mathrm{d}v_i^s}{\mathrm{d}t}+\sigma^s_{ij,j}-\sigma^f_{ij,j}+(\rho^s-\rho^f)g_i \quad \forall \mathbf{x}^s \in \Omega^s \tag{2}$$

The FSI force is calculated based on a force balance in the updated Lagrangian solid domain, Equation (2), and it is treated as an additional body force acting on the fluid, Equation (3). Note that, for brevity, we ignored in Equation (2) the fluid stress within the solid domain. Details on the weak form of Equation (2) can be found in Zhang and Gay [24].

DOI: 10.1002/fld

2.3.2. Computational domain. In the IEFGM, the Eulerian incompressible Newtonian fluid is described using the Navier–Stokes equations. The real fluid occupies the region $\Omega^{\mathrm{f}} = \Omega/\bar{\Omega}$, i.e. the entire computational domain minus the overlapping domain. As done in Li and Liu [1], Zhang and Gay [24], and Zhang *et al.* [25], the momentum equation for the entire computational domain (real fluid plus artificial fluid) can be obtained by combining the Navier–Stokes equation for the real fluid and the interaction force as

$$\rho^{\mathrm{f}} \frac{\mathrm{d}v_i}{\mathrm{d}t} = \sigma^{\mathrm{f}}_{ij,j} + f_i^{\mathrm{FSI}} \quad \forall \mathbf{x} \in \Omega \tag{3}$$

In Equation (3), we assume that no external force has been applied to the fluid domain. Note that the only difference between this and the Navier–Stokes equation is the last term on the right-hand side, namely f_i^{FSI}. This term accounts for the 'extra' artificial fluid contained in the overlapping domain and, in the IEFGM formulation, it has a non-zero value inside the overlapping region and its immediate surroundings. Its value decreases to zero at places outside the region.

The two interaction forces f_i^{FSI} and $f_i^{\mathrm{FSI,s}}$ constitute an action–reaction force pair. The force $f_i^{\mathrm{FSI,s}}$ acts upon the solid domain and it is defined in Equation (2). On the other hand, the force f_i^{FSI} acts upon the artificial fluid inside the overlapping domain and it is obtained by distributing $f_i^{\mathrm{FSI,s}}$ from the solid domain to the computational fluid domain. The way in which we approach this distribution is a central point of this work and it is explained in Section 2.4.2.

Since we consider the whole computational domain Ω to be incompressible, we apply the incompressibility constraint as

$$v_{i,i} = 0 \quad \forall \mathbf{x} \in \Omega \tag{4}$$

Equations (3) and (4), with the variables defined using an Eulerian formalism, represent the strong forms of the governing equations for the entire computational domain ($\Omega^{\mathrm{f}} \cup \bar{\Omega} = \Omega$). A FEM with a penalty formulation to impose incompressibility in the fluid domain and a Petrov–Galerkin technique to treat the advection term [28] were used to solve these equations. In this work, a temperature distribution within the fluid domain was calculated by coupling the energy equation to the FSI problem in an explicit manner. The solid region, in contrast, was assumed to be in thermal equilibrium with the fluid at all times.

2.4. Coupling between the solid and fluid domains

A critical point in the development of a numerical code capable of simulating fluid–structure interaction problems with the IEFGM formulation is the coupling between the fluid and solid domains. Two critical variables relevant to this coupling are the solid domain velocity $\mathbf{v}^{\mathrm{s}}(\mathbf{x}, t)$ and the interaction force acting upon the artificial fluid in the overlapping domain $\mathbf{f}^{\mathrm{FSI}}$.

2.4.1. Solid domain velocity $\mathbf{v}^{\mathrm{s}}$. We consider a no-slip condition between the solid and the overlapping domains. Moreover, since the discretizations of the solid and fluid regions are independent, the nodes of the Eulerian grid in the computational domain will, in general, not coincide with the moving particles of the solid domain at every time step. Therefore, a coupling between the fluid nodal velocity $\mathbf{v}(\mathbf{x}, t)$ and the solid particles velocity $\mathbf{v}^{\mathrm{s}}(\mathbf{x}, t)$ is needed. This coupling is accomplished by means of a local approximation of the fluid velocity field.

In Figure 2 a schematic representation of the local approximation of the x-component of the fluid nodal velocity field (v_x) is shown. The dots represent the nodal values of the fluid velocity

DOI: 10.1002/fld

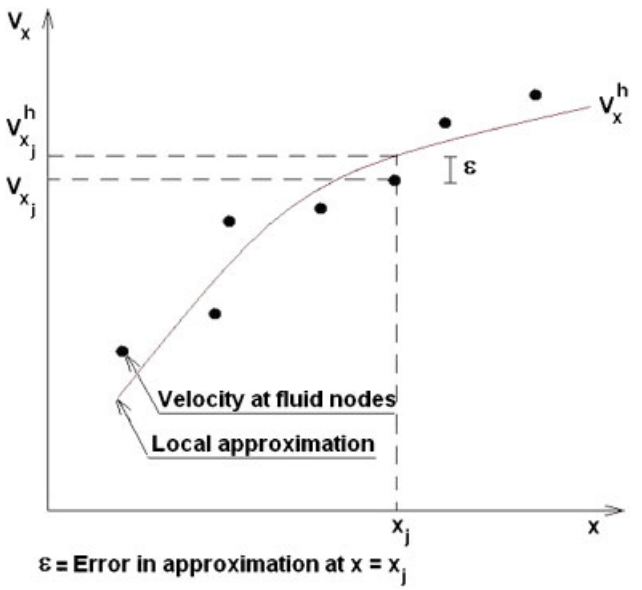

Figure 2. Schematic representation of the local approximation of the x-component of the fluid nodal velocity (v_x). The dots represents the velocity at different nodes in the Eulerian fluid mesh. The solid curve represents the local approximation of the x-component of the fluid velocity field.

and the solid curve represents the approximated continuum velocity field (v_x^{h}). The approximation is done by means of the MLS procedure. Several authors [27, 29] have used the MLS procedure to approximate a set of scattered data. Following the minimization procedure described in Dolbow and Belytschko [30], the approximated velocity field may be expressed as

$$\mathbf{v}^{\mathrm{h}}(\mathbf{x}) = \sum_{j}^{n} \phi_j(\mathbf{x}) \mathbf{v}(\mathbf{x}_j, t) \quad \forall \mathbf{x}_j \in \Omega_x \tag{5}$$

where the MLS shape functions are defined as

$$\phi_j(\mathbf{x}) \stackrel{\mathrm{def}}{=} \mathbf{p}^{\mathrm{T}}(\mathbf{x}) \cdot \left[\sum_{i=1}^{n} w(\mathbf{x}-\mathbf{x}_i) \cdot \mathbf{p}(\mathbf{x}_i) \cdot \mathbf{p}^{\mathrm{T}}(\mathbf{x}_i) \right]^{-1} \cdot w(\mathbf{x}-\mathbf{x}_j) \cdot \mathbf{p}(\mathbf{x}_j) \tag{6}$$

Since we are considering a no-slip condition between the fluid and solid domains, we can write

$$\mathbf{v}^{\mathrm{s}}(\mathbf{x} = \mathbf{v}^{\mathrm{h}}(\mathbf{x}) \quad \forall \mathbf{x} \in \Omega^{\mathrm{s}} \equiv \bar{\Omega} \tag{7}$$

For a solid particle at current position $\mathbf{x}^{\mathrm{s}}(t)$, an influence domain Ω_x that covers a subset of n fluid nodes j positioned at x_j is constructed. Using Equations (5), (6) and (7), the velocity for the solid particle is then obtained from the velocities at fluid nodes within Ω_x. A detailed explanation of the method used to estimate the size of the influence domain is presented in Liu [3].

2.4.2. Distribution of the interaction force, $\mathbf{f}^{\mathrm{FSI}}$*, in the fluid domain.* Equation (2) gives the FSI force at each solid particle's position. To distribute this force onto the fluid nodes, we used the

DOI: 10.1002/fld

same approach as for the velocity field approximation in the solid domain, i.e. the MLS procedure. The local approximation of the interaction force can be expressed as

$$f_i^{\mathrm{FSI,s}}(\mathbf{x}^{\mathrm{s}}) = \sum_j^n \Phi_j(\mathbf{x}^{\mathrm{s}}) f_i^{\mathrm{FSI,s}}(\mathbf{x}_j^{\mathrm{s}}) \quad \forall \mathbf{x}_j^{\mathrm{s}} \in \Omega_{x^{\mathrm{s}}} \tag{8}$$

As mentioned in Section 2.3.2, the two interaction forces f_i^{FSI} and $f_i^{\mathrm{FSI,s}}$ constitute an action and reaction force pair; hence, they must be equal in magnitude and act in opposite directions.

$$f_i^{\mathrm{FSI}}(\mathbf{x}) = -f_i^{\mathrm{FSI,s}}(\mathbf{x}) \quad \forall \mathbf{x} \in \bar{\Omega} \tag{9}$$

When distributing the FSI force, a fluid node may fall inside the influence domain of more than one solid particle (n in Equation (8)). Therefore, the interaction force at each solid node contributes in part to the interaction force at each surrounding fluid node.

2.4.3. Updating the position of the solid particles. Since we are considering a current Lagrangian description for the solid domain, the position of the solid particles can be updated from the solid velocity calculated in Equation (7):

$$x_i^{\mathrm{s},n+1} = x_i^{\mathrm{s},n} + v_i^{\mathrm{s},n+1} = \Delta t \tag{10}$$

where the index $n+1$ indicates quantities evaluated at the current time step and Δt is the time step size.

2.5. Algorithm

In this section we summarize the assumptions made for the fluid and the solid domain and the proposed algorithm. The assumptions made are the following:

(a) The fluid is incompressible.
(b) The solid is incompressible.
(c) The solid must remain immersed in the fluid at all times during the simulation.
(d) No-slip condition between the solid and fluid domains.

The algorithm for the IEFGM can be outlined as follows:

(a) Set the initial position of all the solid particles at time $t=0(\Omega_0^{\mathrm{s}})$.
(b) Calculate the fluid–solid interaction force $f_i^{\mathrm{FSI,s}}$ on the solid particles using Equation (2).
(c) Distribute the solid–fluid interaction force from the solid domain onto the fluid domain (from $f_i^{\mathrm{FSI,s}}$ to f_i^{FSI}) using Equations (6), (8), and (9).
(d) Approximate the solid velocity $\mathbf{v}^{\mathrm{s}}$ using Equations (5), (6), and (7).
(e) Update the positions of the solid particles using Equation (10).
(f) Solve for the fluid velocities and pressure distribution using Equations (3) and (4).

2.5.1. Important points.

- The fact that the interaction force f_i^{FSI} is added in an explicit manner into the Navier–Stokes equation for the fluid, Equation (3), restricts the size of the time step to be used. The more rigid the solid material, the smaller the time step needed for convergence. In all the cases of study presented in this work, a time step of $1.0\mathrm{e}-4\,\mathrm{s}$ had to be used.

DOI: 10.1002/fld

- According to Zhang and Gay [24], the spacing of the fluid grid has to be approximately two times larger than the spacing of the background solid mesh to avoid fluid sinking through into the solid domain. It is appropriate to maintain the fluid grid larger than the solid background grid but not too large because it may cause a decrease in accuracy. Note that even though in this work the solid is being modeled using the element-free Galerkin (EFG) mehfree method, as detailed in Dolbow and Belytschko [30], we still need a background grid in the solid region for the integration of the weak form of the governing equations.

3. NUMERICAL EXAMPLES

In this work, we study four two-dimensional numerical examples to explore the capability and performance of the IEFGM formulation. All the simulated examples consist of the same geometrical configuration, a soft solid disk (0.2 mm in diameter) moving in a viscous fluid (a 20 mm high by 5 mm wide domain) due to the action of the gravitational force and due to a fluid's velocity field produced by thermal convection. The difference between the cases lies in the different values of the solid's density and the solid's Young's modulus considered. Moreover, in all four cases, we assumed the solid to be an incompressible elastic material governed by Hooke's constitutive law.

The authors recognize that for structures with large deformations a more suitable constitutive model, like a Mooney–Rivlin material description, should be used. Nonetheless, the main objective of this work is to show the capabilities of the method to handle large deformations without focusing for now on the real material response. In a future work, where this technique will be applied to simulate defects in casting processes caused by deformable oxide films [31], a more realistic constitutive model will be considered.

The fluid and solid's geometrical and material properties are summarized in Table I. The properties of the fluid are similar to those of a Pb–Sn liquid metal. Although not presented in this work, we will extend the current model to simulate the transport of inclusions during solidification of alloys.

The temperature initial and boundary conditions are the same for all cases studied. We consider for the fluid domain an initial temperature $T_i = 550\,K$ and a constant temperature boundary condition $T_o = 600\,K$ on the right vertical boundary, i.e. $\forall \mathbf{x} \in \{x = 5\,mm, 0 \leqslant y \leqslant 10\,mm\}$. The computational domain is thermally insulated on the other three boundaries. Non-slip boundary conditions are considered on all solid boundaries. In Figure 3, the temperature boundary conditions for the computational domain and the two initial positions of the solid domain considered in this work are shown.

Table I. Geometrical and material properties of the fluid and solid domains.

	Fluid domain	Circular solid domain
w (m)	0.01	—
h (m)	0.02	—
d (m)	—	200e−6
$\rho(kg/m^3)$	8800	8800/9700
$\mu(Ns/m^2)$	2e−3	—
$E(N/m^2)$	—	10/1000/3000
v	—	0.3

DOI: 10.1002/fld

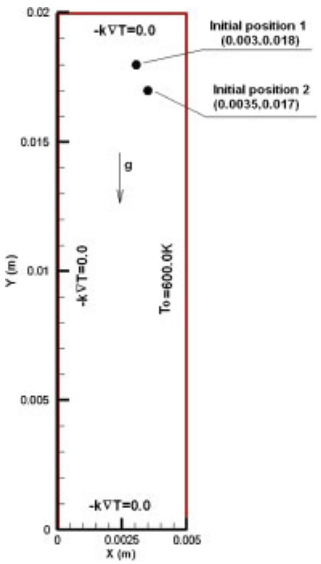

Figure 3. Two-dimensional computational domain considered, with the corresponding temperature boundary conditions and the two solid's initial positions reckoned in this work.

The Eulerian and Lagrangian grids are obtained using Hypermesh [32]. To assure an appropriate integration at all times, the Lagrangian-background grid is independent of the position of the particle discretization. An adaptive meshing scheme is introduced, which refines the Eulerian grid locally near the position of the solid domain and is computationally inexpensive since the Eulerian and Lagrangian-background grids are generated independently. It is important to note that the Eulerian grid is comprised only of quadrilateral elements. Although a triangular grid would be more suitable for adaptive refinement, the current flow solver formulation (based on the penalty method) requires rectangular elements. An implementation using adaptive re-meshing with triangular elements based on the fractional step formulation will be reported elsewhere. An example of the Eulerian and Lagrangian (background) grids used is shown in Figure 4.

In FEM, the integration grid is the same as the element grid. To obtain accurate results, the element grid must be sufficiently fine and a sufficient number of integration points per element must be used. In EFG, however, the background integration grid is required only in performing the integration of computing the stiffness matrix, and its re-meshing can be done independently (up to a certain extent) of the movement of the particles [3].

3.1. Case I

The solid and fluid's properties considered for this case are summarized in Table I. Specifically, we consider a solid's density $\rho^{\mathrm{s}} = \rho^{\mathrm{f}} = 8800\,\mathrm{kg/m^3}$ and a Young's modulus $E = 3000\,\mathrm{N/m^2}$. The initial position of the Lagrangian solid domain is $\mathbf{x} = (0.003\,\mathrm{m}, 0.018\,\mathrm{m})$, and it is indicated as 'Initial position 1' in Figure 3. In this case of study, we allow heat conduction within the fluid domain for 1 s before immersing the solid body. Therefore, by the time the solid is immersed, there is a non-constant temperature distribution and a corresponding velocity field, due to fluid

DOI: 10.1002/fld

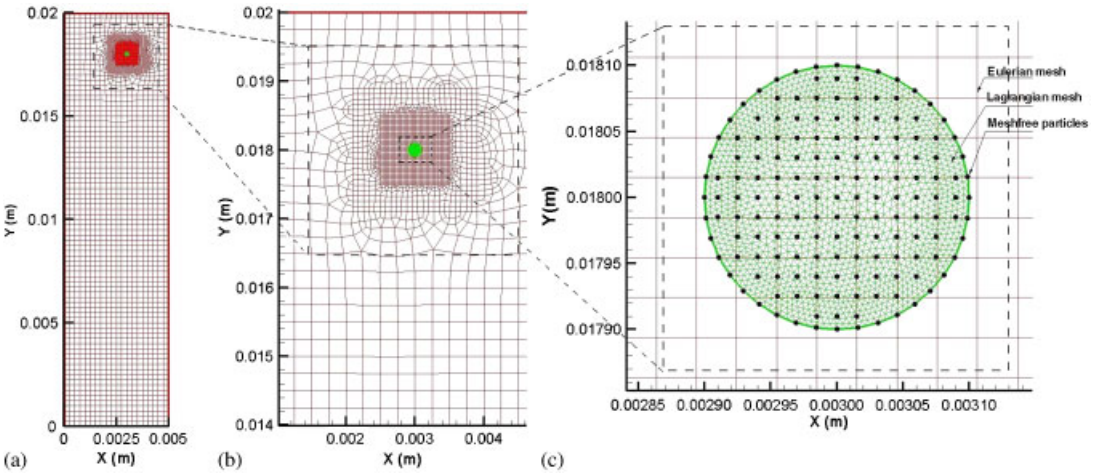

Figure 4. Comparison between the different scales involved in this problem. Both the Eulerian and the Lagrangian meshes are implemented using Hypermesh. The Lagrangian solid will always be inside the refined zone of the Eulerian mesh.

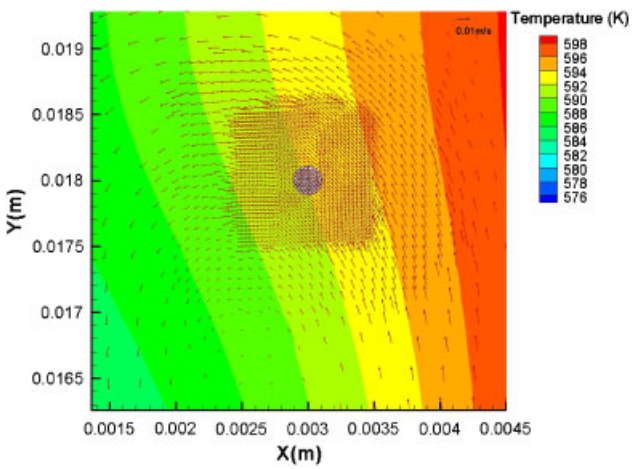

Figure 5. Initial condition under which the solid body was immersed. The temperature distribution and velocity field were obtained by allowing heat conduction, and the subsequent thermal convection, within the fluid domain during 1 s prior to the immersion of the solid body. The solid body is shown to indicate its initial position.

thermal convection, within the fluid. The initial condition under which the solid body is immersed is shown in Figure 5.

Throughout the simulation, the temperature of the fluid increases as a result of heat being transferred from the right wall.

One question we can ask ourselves is whether under these conditions the FSI will cause fluid recirculation along the fluid–structure interface. We address this question by considering Figure 6. In Figure 6(a), the trajectory followed by the solid body is presented. The background corresponds

DOI: 10.1002/fld

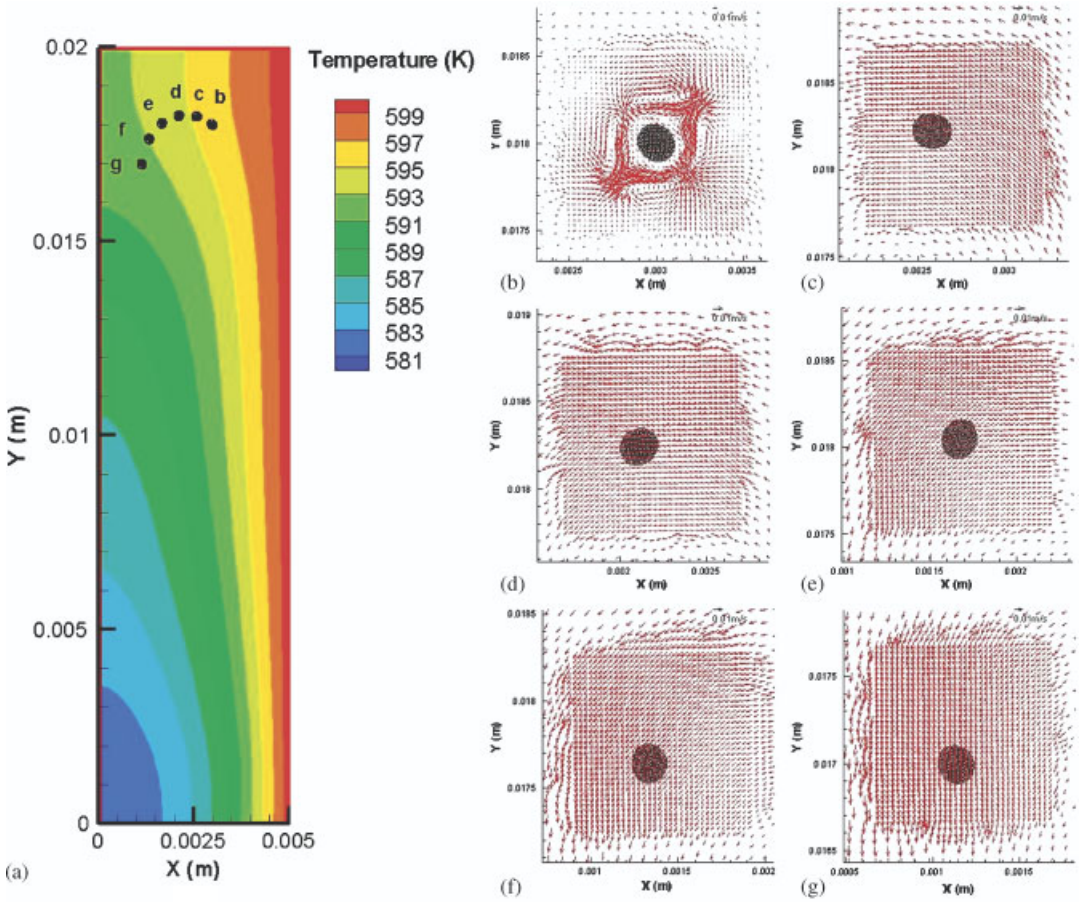

Figure 6. (a) Trajectory followed by the solid body at different times and fluid's temperature distribution at time $t_g = 0.67$ s. Fluid's velocity field, shape, and position of the solid body at: (b) 0.0006 s; (c) 0.084 s; (d) 0.162 s; (e) 0.24 s; (f) 0.32 s; and (g) 0.40 s.

to the temperature field at time $t_f = 0.40$ s. Also, a detail of the fluid's velocity field and the shape and position of the solid domain are presented at six different times in Figures 6(b) thorough (g), correspond to times $t_b = 0.0006$ s, $t_c = 0.084$ s, $t_d = 0.162$ s, $t_e = 0.24$ s, $t_f = 0.32$ s, and $t_g = 0.40$ s, respectively.

The analysis of the fluid's velocity fields shown allows us to state that, in this particular problem, the presence of the solid generates an initial recirculation, Figure 6(b), which we refer to as 'transitional velocity field' in this work. This complex transitional field is produced by the resistance of the solid body to the shear strain initially imposed by the fluid. Moreover, since we are considering an incompressible elastic solid material governed by Hooke's constitutive law, the resistance of the solid body to the initial shear is directly proportional to its Young's modulus E. Therefore, the higher the value of E, the larger this resistance will be, causing a stronger transitional velocity field. This effect can be seen in Figure 7, where the effect of different values of Young's modulus on the transitional velocity field is shown.

DOI: 10.1002/fld

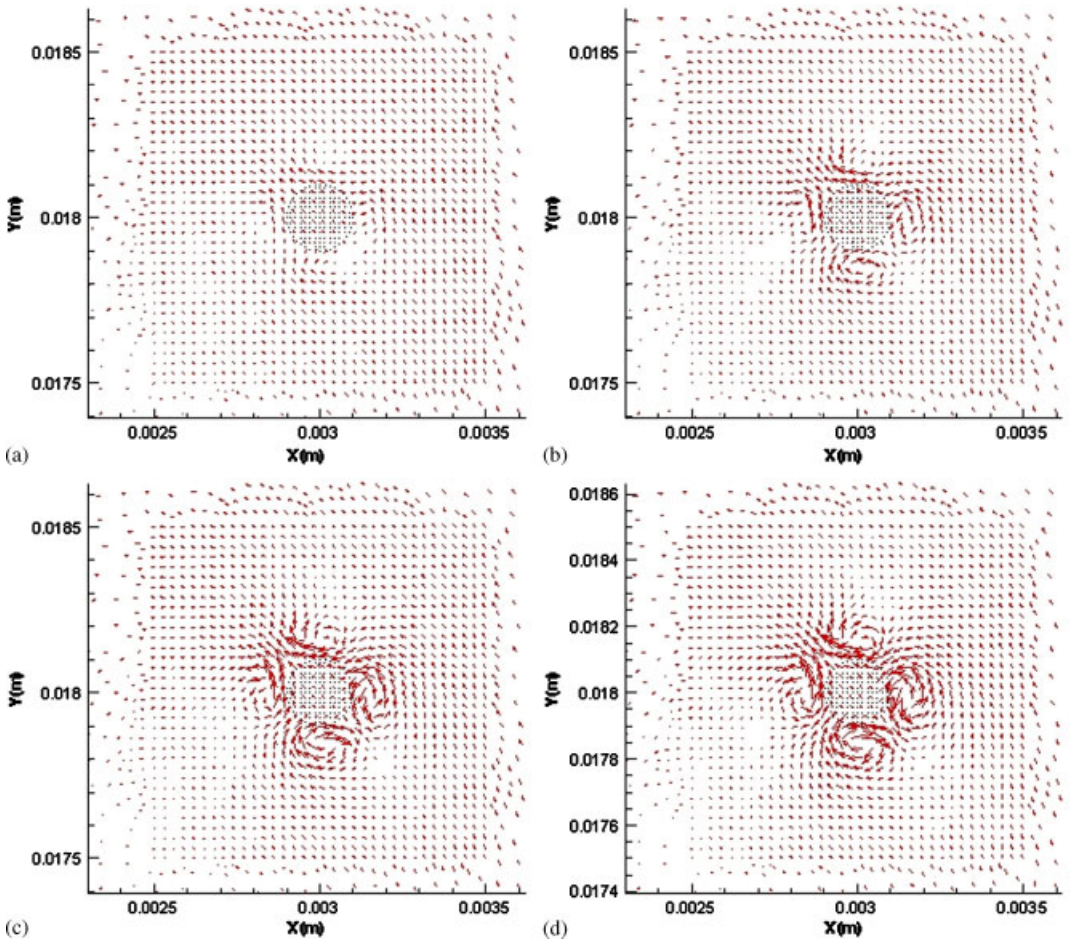

Figure 7. Transitional velocity field obtained at time $t = 6.0\text{e}-5\,\text{s}$ after the solid body was immersed. These cases correspond to different values of Young's modulus, in particular: (a) $E_\text{a} = 200\,\text{N/m}^2$; (b) $E_\text{b} = 500\,\text{N/m}^2$; (c) $E_\text{c} = 800\,\text{N/m}^2$; and (d) $E_\text{d} = 1000\,\text{N/m}^2$.

It is important to note that the transitional velocity field rapidly smoothes out, in fact, from $t_\text{c} = 0.084\,\text{s}$, Figures 6(c) through (g), no fluid recirculation is observed. The reason that the FSI seems not to generate fluid recirculation after the transition lies in the fact that, in this case, the solid and fluid densities are the same ($\rho^\text{s} = \rho^\text{f} = 8800\,\text{kg/m}^3$). Therefore, the difference between the buoyancy of the fluid in the overlapping domain and the weight of the solid is zero, and the 'extra' inertial force (when compared with the inertial force of the fluid in the overlapping domain) introduced by the solid is also zero. This makes the terms $(\rho^\text{s} - \rho^\text{f})g_i$ and $(\rho^\text{s} - \rho^\text{f})\text{d}v_i^\text{s}/\text{d}t$ in Equation (2) equal to zero. The interaction force can then be rewritten as

$$f_i^{\text{FSI,s}} = \sigma_{ij,j}^\text{s} \quad \forall \mathbf{x}^\text{s} \in \Omega^\text{s} \tag{11}$$

As we can see in Equation (11), only the solid's state of stress contributes to the interaction force. Therefore, the only way in which, under these conditions, the FSI could cause fluid recirculation

DOI: 10.1002/fld

would be for the solid to resist a high displacement gradient imposed by the fluid. The resistance would increase the value of the solid's stress tensor, increasing the interaction force $f^{\mathrm{FSI,s}}$, and generating, as a consequence, a zone of high pressure in the fluid that would cause the correspondent fluid recirculation. Nonetheless, since the length scale of the solid domain is much smaller than the length scale of the computational domain, the gradient of displacement imposed by the fluid onto the solid body is small. This means that all the solid particles move approximately in the same direction. Therefore, this small displacement gradient does not cause a high resistance from the solid, preventing the recirculation vortex in the fluid from originating.

In Figure 8, a detailed close-up of the solid's final shape and the fluid's final velocity field is shown. We can see that, as mentioned before, fluid recirculation is not produced and the gradient of displacement within the solid is small (all the solid particles move in approximately the same direction). As a consequence, the solid is not greatly distorted.

In Figures 7(b) through (f) we can see that, after the transition, the solid moves along the streamlines of the velocity field. A closer examination of the solid's trajectory in Figure 9 reveals that the solid not only translates, but it also rotates in a counterclockwise direction.

The red dots and the blue squares in this figure correspond to the centroid of the solid and the position of the solid particle number one at every time step, respectively. A line segment connecting each red dot with its corresponding blue square represents a small solid fiber that helps to visualize the solid's rotation.

For clarity, in Figure 9 the position and shape of the solid at 12 different times (from right to left 0.0048 s, 0.041 s, 0.077 s, 0.112 s, 0.150 s, 0.185 s, 0.221 s, 0.257 s, 0.292 s, 0.329 s, 0.365 s, and 0.400 s) are shown.

To understand the rotation of the solid, we refer to Figure 10. In this figure, the solid body, fluid's velocity field, and a contour plot of the x-component of fluid's velocity field at time $t = 0.112$ s

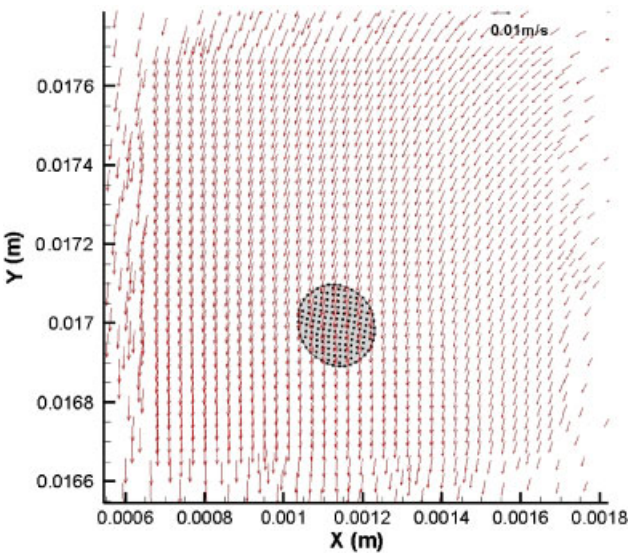

Figure 8. Velocity field and Lagrangian solid at time $t = 0.40$ s. A detailed close-up of the final shape of the solid and the final velocity field is shown.

DOI: 10.1002/fld

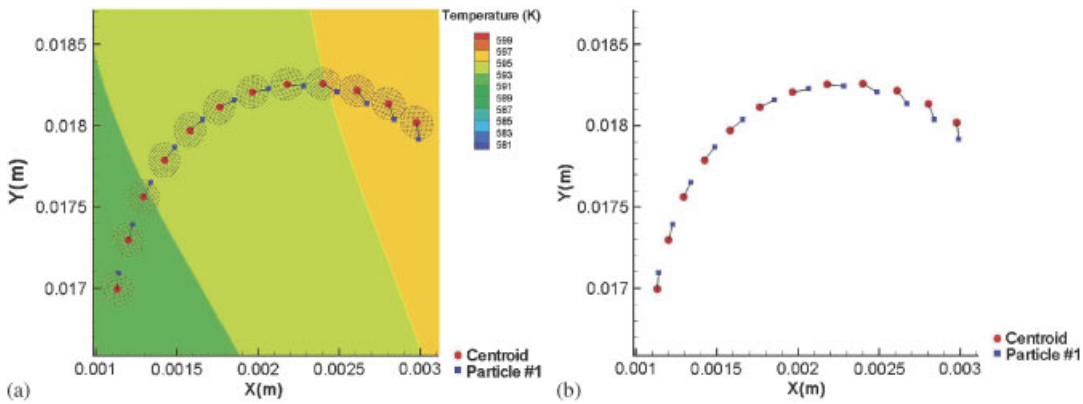

Figure 9. (a) Position and shape of the solid body at 12 different times are shown. The red dots represent the centroid of the solid body, whereas the blue squares represent the position of the solid particle number 1. The line segments connecting the red dots and the corresponding blue squares at each time represent small solid fibers. The background corresponds to the temperature distribution at $t = 0.400$ s and (b) the centroids, the positions of particle number 1, and the small fibers of the solid body are shown. The different times are, from right to left, 0.0048 s, 0.041 s, 0.077 s, 0.112 s, 0.150 s, 0.185 s, 0.221 s, 0.257 s, 0.292 s, 0.329 s, 0.365 s, and 0.400 s.

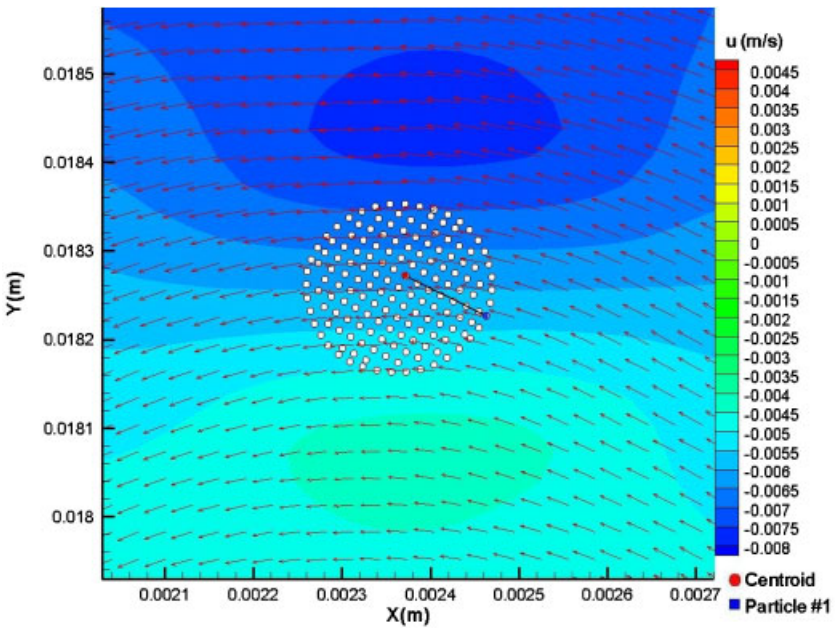

Figure 10. Velocity field and the Lagrangian solid at time $t = 0.112$ s. The contour plot corresponds to the x-component of the velocity field (u). At this particular time the solid body is approximately moving only in the negative x-direction.

DOI: 10.1002/fld

(fourth solid position from right to left in Figure 9) are shown. As mentioned before, the solid body moves along the streamlines of the velocity field. At time $t=0.112\,\mathrm{s}$, the streamlines along which the solid is moving span almost entirely along the x-direction. This means that, at this particular time, the solid body is translating only in the horizontal direction. The contour plot of the x-component of the velocity field shows that the upper part of the body is moving faster than the lower part, causing a combined movement of translation and rotation in a counterclockwise direction. This explanation may be extended to every time step acknowledging that the solid will always move along the streamlines of the velocity field. Since the time difference between each solid's position and its successor in Figure 9 is always the same, $\Delta t=0.036\,\mathrm{s}$, it can be noticed that the solid is not only translating and rotating, but it is also accelerating.

3.2. Case II

One of the main objectives of this work is to show the capabilities of the IEFGM to deal with large deformations of the solid body in FSI problems. In order to increase the deformation of the solid, with respect to the previous results, in this case we increase the value of the solid's density and decrease the value of Young's modulus. Here we consider $\rho^{\mathrm{s}}=9700\,\mathrm{kg/m3}$ and $E=1000\,\mathrm{N/m^2}$. We solve the problem with the same geometrical configuration and boundary conditions as in case I. The initial position of the Lagrangian solid domain is $\mathbf{x}=(0.003\,\mathrm{m},\,0.018\,\mathrm{m})$, and it is indicated as 'Initial position 1' in Figure 3. Also, the initial fluid's temperature and velocity fields in which the solid body is immersed are the same as in case I and are shown in Figure 5.

In comparison with the previous results, Figures 11(b) through (f) show that in this case the solid undergoes a larger deformation and fluid recirculation appears after the initial transitional fluid velocity field.

Since in this problem the solid's density is higher than the fluid's density ($\rho^{\mathrm{f}}=8800\,\mathrm{kg/m^3}$ and $\rho^{\mathrm{s}}=9700\,\mathrm{kg/m^3}$), the buoyancy force on the solid is lower than its weight. Therefore, the solid not only follows the thermal convective velocity field, but it also falls by gravity. This causes the solid to accelerate inside the fluid domain, with the consequent solid deformation. The smaller value of Young's modulus reduces solid's stiffness, allowing a larger deformation (the final shape of the solid can be seen in Figure 12). Moreover, as the solid sinks deeper into the fluid and resists, to some extent, the deformation imposed by fluid's velocity field, local zones of high pressure are generated in the fluid domain causing the correspondent fluid recirculation.

In Figure 13 it can be seen that, in its movement, the solid not only translates but it also rotates. The rotation can be understood using the same principles explained in case I. Nevertheless, it is important to note that, while in case I the rotation was always in a counterclockwise direction, in this case the fluid recirculation produces a complex velocity field that causes the solid's rotation to alternate between a counterclockwise and a clockwise direction (see Figure 13). The translation and rotation of the solid imposed by the complex fluid's velocity field contributes to the asymmetrical large deformation of the solid body.

3.3. Case III

In order to obtain a larger deformation of the solid domain in a shorter time, compared with the previous cases, we further lower Young's modulus. In this case, we consider $\rho^{\mathrm{f}}=8800\,\mathrm{kg/m^3}$, $\rho^{\mathrm{s}}=9700\,\mathrm{kg/m^3}$, and $E=10\,\mathrm{N/m^2}$. Acknowledging that Young's modulus of a marshmallow at room temperature is $29000\,\mathrm{N/m^2}$, the notably small value considered here makes this problem

DOI: 10.1002/fld

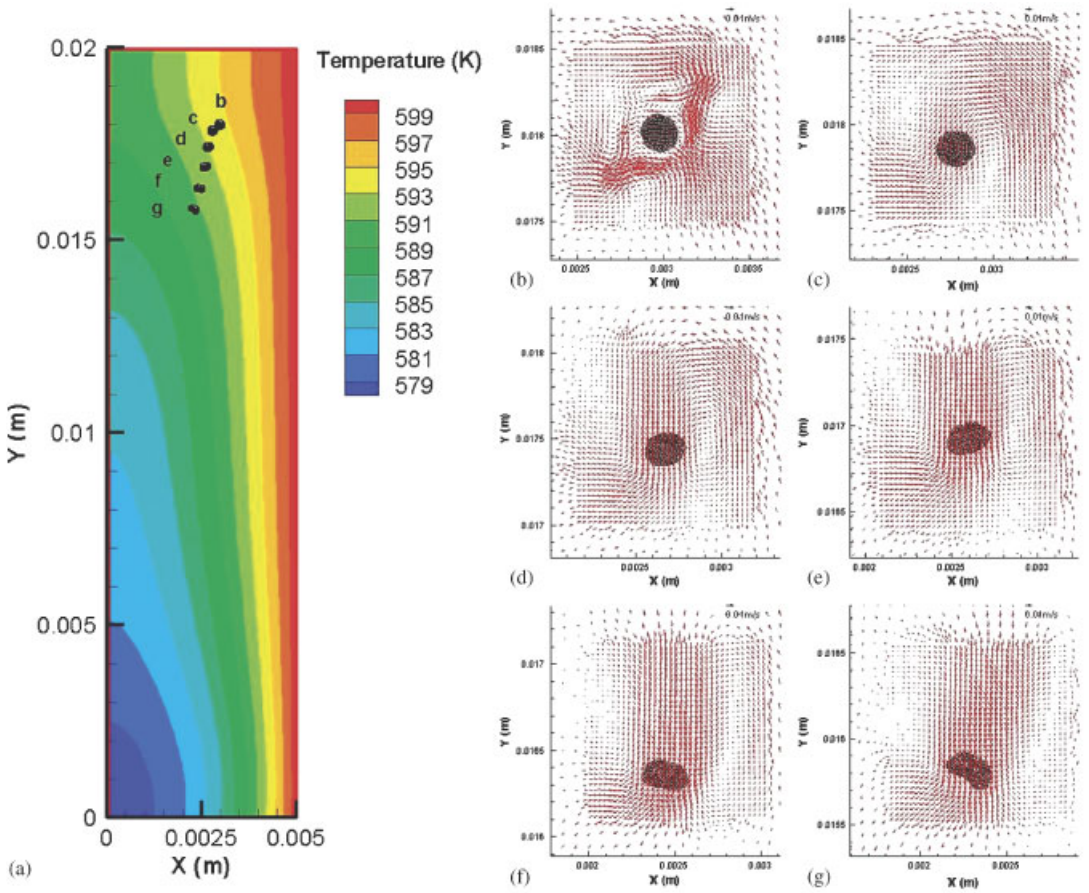

Figure 11. (a) Trajectory followed by the solid body at different times and fluid's temperature distribution at time $t_g = 0.36\,s$ and (b) fluid's velocity field, shape, and position of the solid body at (b) $t_b = 0.0048\,s$; (c) $t_c = 0.047\,s$; (d) $t_d = 0.089\,s$; (e) $t_e = 0.131\,s$; (f) $t_f = 0.173\,s$; and (g) $t_g = 0.215\,s$, respectively.

solely a numerical test to illustrate the large solid deformations that the IEFGM can handle. The initial position of the Lagrangian solid domain is the same as in cases I and II, $\mathbf{x} = (0.003\,m, 0.018\,m)$, and it is indicated as 'Initial position 1' in Figure 3. Also, the initial temperature profile and fluid velocity field in which the solid body is immersed are the same as in case I and are shown in Figure 5.

In Figure 14(a), the general trajectory followed by the solid body at four different times and the temperature field at time $t_e = 0.083\,s$ are shown. Also, a detail of fluid's velocity field and the shape and position of the solid body at times $t_b = 0.0048\,s$, $t_c = 0.041s$, $t_d = 0.059\,s$, and $t_e = 0.083\,s$ are shown in Figures 14(b) through (e), respectively. An important point to note in Figure 14(a) is that, for this case, we do not obtain a transition velocity field as in the previous cases I and II (Figures 6(a) and 11(a)). As mentioned before, the transitional field is the result of the resistance of the solid body to the shear strain initially imposed by the fluid, and it is directly proportional to Young's modulus. As shown in Figure 7(a), the transition effect decreases when the value of E

DOI: 10.1002/fld

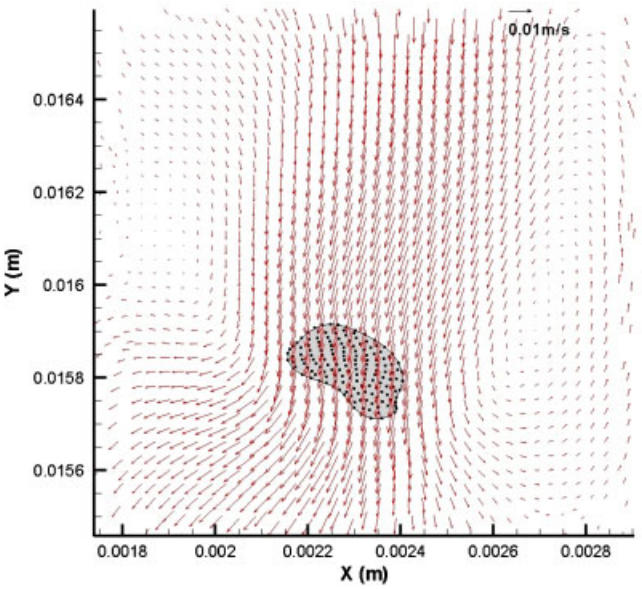

Figure 12. Velocity field and the Lagrangian solid at time $t = 0.215\,\mathrm{s}$. A detailed close-up of the final shape of the solid and the final velocity field is shown.

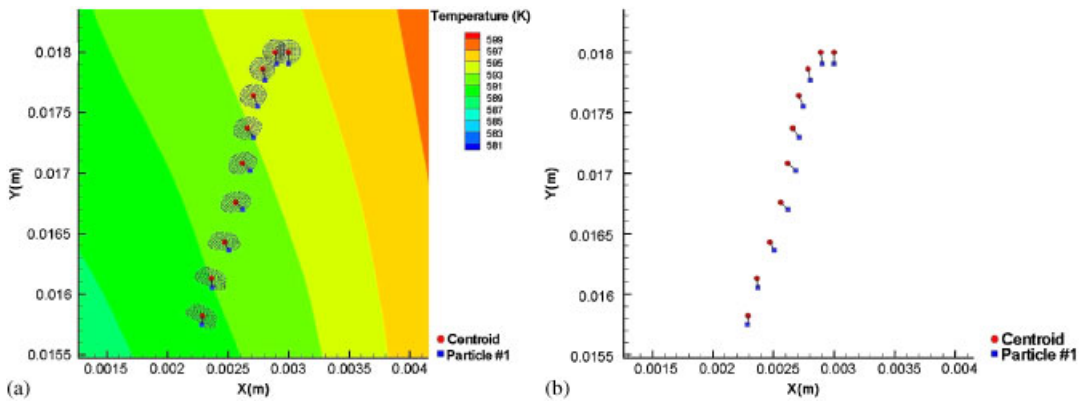

Figure 13. (a) The position and shape of the solid body at 10 different times are shown. The red dots represent the centroid of the solid body, whereas the blue squares represent the position of the solid particle number 1. The line segments connecting the red dots and the corresponding blue squares at each time represent small solid fibers. The background corresponds to the temperature distribution at $t = 0.36\,\mathrm{s}$ and (b) the centroids, the positions of particle number 1, and the small fibers of the solid body are shown. The different times are, from right to left, 0.0 s, 0.023 s, 0.047 s, 0.071 s, 0.095 s, 0.119 s, 0.143 s, 0.167 s, 0.191 s, and 0.215 s.

decreases and it is almost unnoticeable for $E = 200\,\mathrm{N/m^2}$. Since in this problem we are considering $E = 10\,\mathrm{N/m^2}$, the solid offers almost no resistance to the shear strain imposed by the fluid, and therefore no transitional velocity field is observed immediately after the solid is immersed.

DOI: 10.1002/fld

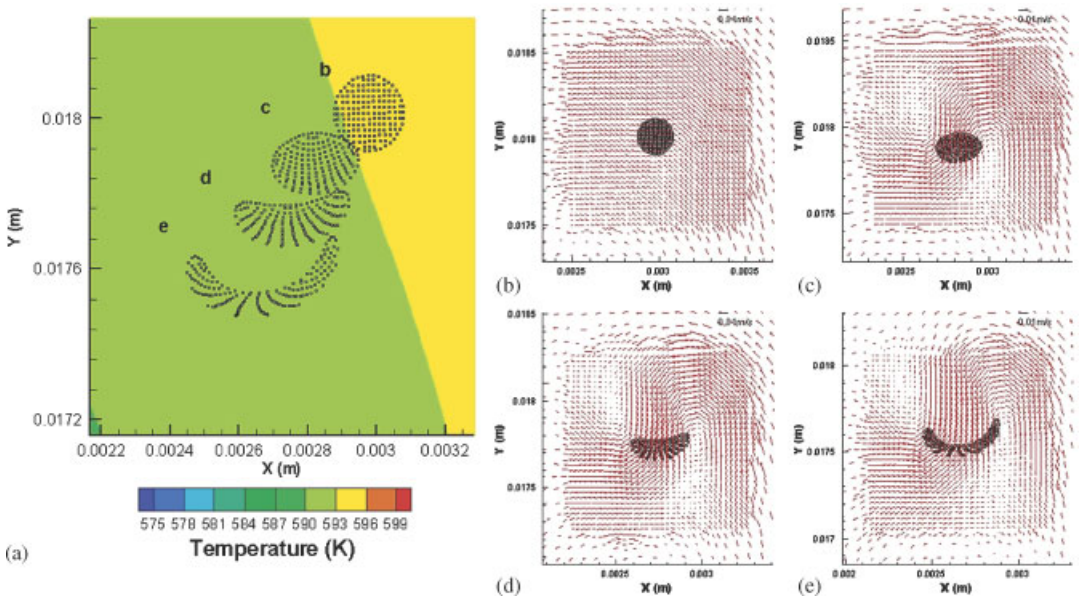

Figure 14. (a) Trajectory followed by the solid body at different times and fluid's temperature distribution at time $t_e = 0.083$ s and (b) fluid's velocity field, shape, and position of the solid body at (b) $t_b = 0.0048$ s; (c) $t_c = 0.041$ s; (d) $t_d = 0.059$ s; and (e) $t_e = 0.083$ s, respectively.

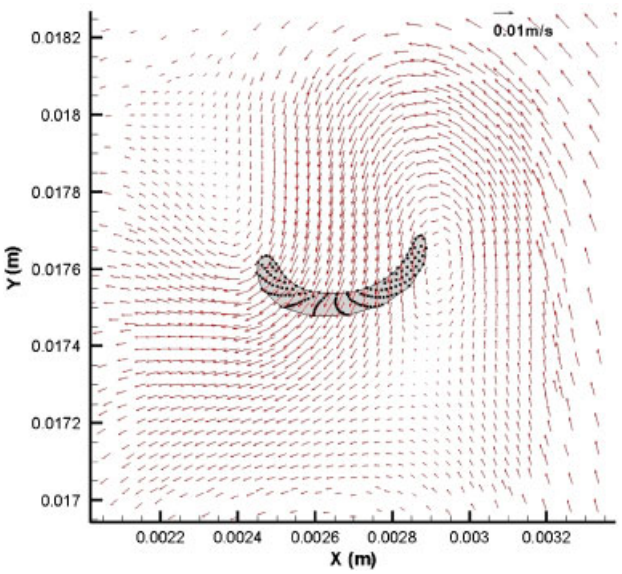

Figure 15. Velocity field and Lagrangian solid at time $t = 0.083$ s. A close-up of the shape of the solid and the velocity field is shown.

DOI: 10.1002/fld

In Figure 14, we can see that, in this case, an extremely large deformation is obtained in a short time (the solid deforms in a great manner after only 0.083 s). A close-up of the shape of the solid and the fluid velocity profile at 0.083 s is shown in Figure 15.

3.4. Case IV

In this case we analyze the movement of a more rigid solid body (compared with the previous cases) with a constant initial temperature distribution ($T_0 = 550\,\mathrm{K}$) and no initial fluid velocity. Here we consider $\rho^{\mathrm{f}} = 8800\,\mathrm{kg/m^3}$, $\rho^{\mathrm{s}} = 9700\,\mathrm{kg/m^3}$, and $E = 3000\,\mathrm{N/m^2}$. The initial position of the solid body is $\mathbf{x} = (0.0035\,\mathrm{m}, 0.017\,\mathrm{m})$, and it is indicated as 'Initial position 2' in Figure 3.

In Figure 16(a), the general trajectory followed by the solid body at nine different times and fluid's temperature field at time $t_{\mathrm{f}} = 0.47\,\mathrm{s}$ are shown. Also, a detail of the fluid's velocity field

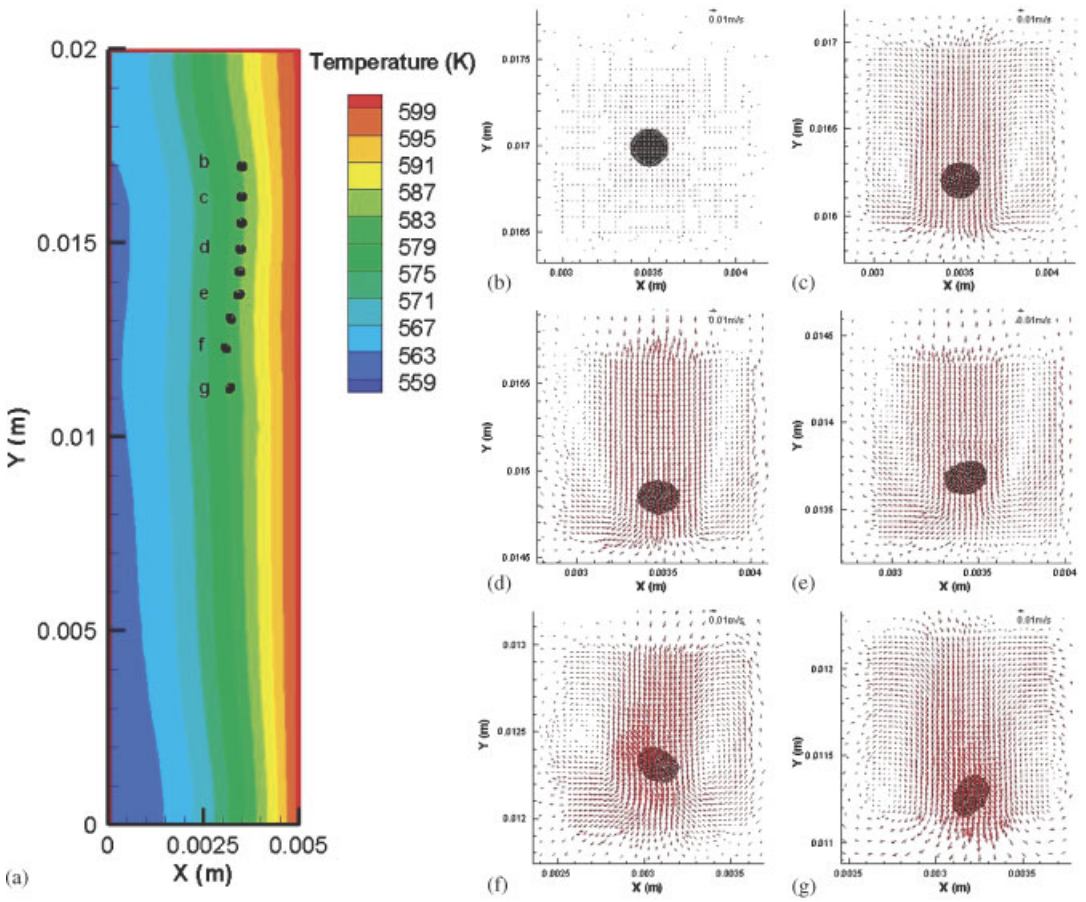

Figure 16. (a) Trajectory followed by the solid body at different times and fluid's temperature distribution at time $t_{\mathrm{g}} = 0.47\,\mathrm{s}$ and (b) fluid's velocity field and shape and position of the solid body at (b) $t_{\mathrm{b}} = 0.01\,\mathrm{s}$; (c) $t_{\mathrm{c}} = 0.1\,\mathrm{s}$; (d) $t_{\mathrm{d}} = 0.2\,\mathrm{s}$; (e) $t_{\mathrm{e}} = 0.3\,\mathrm{s}$; (f) $t_{\mathrm{f}} = 0.4\,\mathrm{s}$; and (g) $t_{\mathrm{g}} = 0.47\,\mathrm{s}$, respectively. Some other solid's positions are shown in (a) to better understand its general trajectory.

DOI: 10.1002/fld

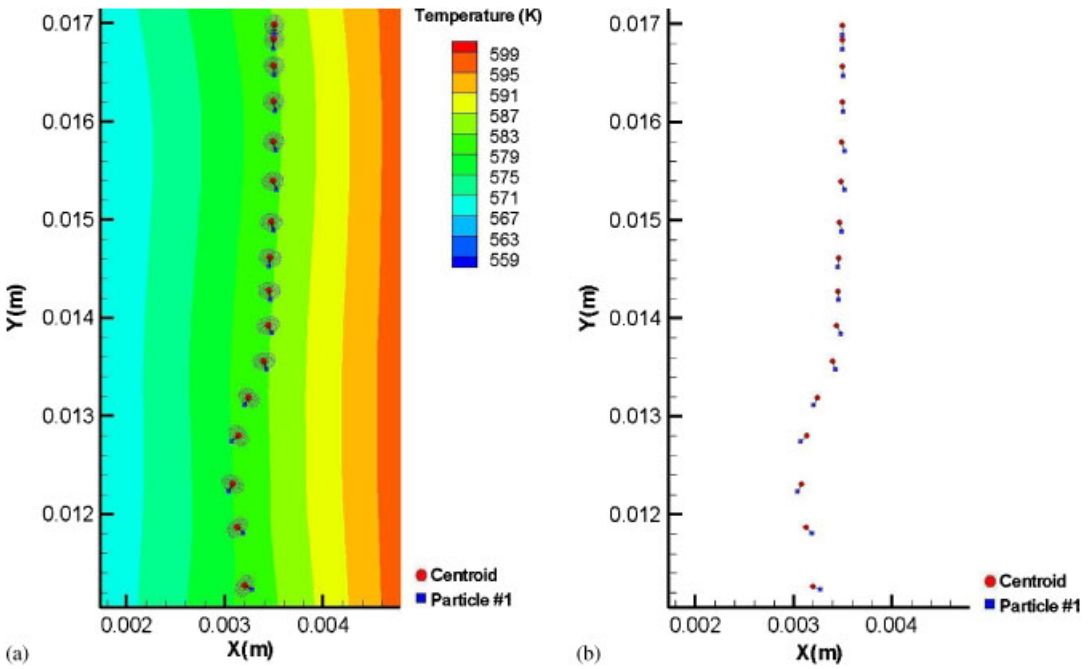

Figure 17. (a) Position and shape of the solid body at 16 different times are shown. The red dots represent the centroid of the solid body, whereas the blue squares represent the position of the solid particle number 1. The line segments connecting the red dots and the corresponding blue squares at each time represent small solid fibers. The background corresponds to the temperature distribution at $t=0.47$ s and (b) the centroids, the positions of particle number 1, and the small fibers of the solid body are shown. The different times are, from right to left, 0.01 s, 0.04 s, 0.07 s, 0.1 s, 0.13 s, 0.16 s, 0.19 s, 0.22 s, 0.25 s, 0.28 s, 0.31 s, 0.34 s, 0.37 s, 0.40 s, 0.43 s, and 0.47 s.

and the shape and position of the solid body at times $t_b=0.01$ s, $t_c=0.10$ s, $t_d=0.20$ s, $t_e=0.30$s, $t_f=0.40$ s, and $t_g=0.47$ s are shown in Figures 16(b) through (g), respectively. Since in this case we consider the fluid to be stationary at time $t=0.0$ s, no initial transitional velocity field is observed. In this problem, as in the previous cases, the temperature of the fluid domain increases with time due to heat being conducted from the right wall. Also, fluid's velocity field is a combination of the thermal convection and the effect of the FSI.

It can be seen in Figures 16(a) through (c) that for $0.0\text{s}\leqslant t<0.3$ s, the solid mainly falls by gravity. Then the trajectory of the body starts to oscillate in the x-direction as a consequence of the interaction between the deformation and rotation of the solid and the pressure gradient imposed by the thermal convection. In Figure 17, a general view of the translation of the solid as well as its rotation is shown.

4. CONCLUSIONS

The IEFGM was presented and used to solve FSI problems. The method was applied to simulate the movement of a deformable solid in a viscous fluid due to the combination

DOI: 10.1002/fld

of the gravitational force and the velocity field produced by the thermal convection of the fluid. The combination of a meshfree particle method (element-free Galerkin) to model the solid domain and the fluid–structure coupling through MLS interpolants gives the proposed approach a distinct advantage for simulating FSI problems with highly deformable solids. The deformation of the solid body obtained in cases II and III was considerably larger than that presented in previous works. In addition, the method seems suitable for tracking the movement of microscale deformable solids. One potential application of this feature is the simulation of defects in casting processes that are caused by deformable inclusions like oxides or bifilms [31].

The thermal convection of the fluid domain, which represents an important factor affecting the movement of the solid body within the fluid, was introduced. Details of the velocity field and the shape and position of the solid as a function of time, which are difficult to model with finite-element-based formulations, were effectively captured by the IEFGM. In its current form, the explicit treatment of the FSI force in the momentum equations introduces a limitation in the time step size. An implicit approach would be necessary to thoroughly evaluate the method's potential for longer and larger simulations.

NOMENCLATURE

Ω	computational domain
Ω^{f}	fluid domain
Ω^{s}	solid domain
$\bar{\Omega}$	overlapping domain
$\mathbf{x}^{\mathrm{s}}$	solid particles' current position
$\mathbf{x}$	fluid particles' position
$f_i^{\mathrm{FSI,s}}$	ith Cartesian component of the fluid–solid interaction force in the solid domain
f_i^{FSI}	ith Cartesian component of the fluid–solid interaction force in the fluid domain
v_i^{s}	ith Cartesian component of the solid particles' velocity
v_i	ith Cartesian component of the fluid nodes' velocity
ρ^{s}	density of solid
ρ^{f}	density of fluid
σ_{ij}^{s}	Cauchy stress tensor for the solid
σ_{ij}^{f}	Cauchy stress tensor for the fluid
g_i	ith Cartesian component of the acceleration of gravity
np	number of nodes in the fluid Eulerian grid
npL	number of particles in the Lagrangian solid domain
w	cubic spline weight function
$\mathbf{p}(\mathbf{x})$	complete polynomial of order 1
$\mathbf{v}^{\mathrm{h}}$	local MLS approximation of the fluid velocity field
ϕ	MLS shape function
E	Young's modulus
μ	viscosity of the fluid
C_{d}	drag coefficient

DOI: 10.1002/fld

ACKNOWLEDGEMENTS

This work was funded by the National Science Foundation through Grant Number CTS-0553570. The authors gratefully appreciate the support provided by the Center for Advanced Vehicular Systems (CAVS) at Mississippi State University.

REFERENCES

1. Li S, Liu WK. *Meshfree Particle Methods*. Springer: Berlin, Heidelberg, 2004.
2. Belytschko T, Lu YY, Gu L. Element-free Galerkin methods. *International Journal for Numerical Methods in Engineering* 1994; **37**:229–256.
3. Liu GR. *Mesh Free Methods—Moving beyond the Finite Element Method*. CRC Press: Boca Raton, FL, U.S.A., 2003.
4. Gingold RA, Monaghan JJ. Smoothed particle hydrodynamics: theory and application to non-spherical stars. *Monthly Notices Royal Astronomical Society* 1977; **181**:375–389.
5. Lucy LB. A numerical approach to the testing of fusion process. *Astronomical Journal* 1977; **88**:1013–1024.
6. Benz W. Smooth particle hydrodynamics: a review. In *The Numerical Modeling of Nonlinear Stellar Pulsatations*, Buchler JR (ed.). Kluwer: Dordrecht, 1990; 269–288.
7. Monaghan JJ. Why particle methods work. *SIAM Journal on Scientific and Statistical Computing* 1982; **3**(4): 422–433.
8. Libersky LD, Petschek AG. Smooth particle hydrodynamics with strength of materials. Advances in the Free Lagrange Method. *Advances in the Free Lagrange Method*. Lecture Notes in Physics, vol. 395. Springer: Berlin, 1990; 248–257.
9. Libersky LD, Petschek AG, Carney TC, Hipp JR, Allahdadi FA. High strain Lagrangian hydrodynamics. *Journal of Computational Physics* 1993; **109**:67–75.
10. Attaway SW, Heinstein MW, Swegle JW. Coupling of smooth particle hydrodynamics with the finite element method. *Nuclear Engineering and Design* 1994; **150**:199–205.
11. Johnson GR. Linking of Lagrangian particle methods to standard finite element methods for high velocity impact computations. *Nuclear Engineering and Design* 1994; **150**:265–274.
12. Swegle JW, Attaway SW, Heinstein MW, Mello FJ, Hicks DL. An analysis of smooth particle hydrodynamics. *Sandia Report SAND93-2513*, 1994.
13. Wen Y, Hicks DL, Swegle JW. Stabilising SPH with conservative smoothing. *Sandia Report SAND94-1932*, 1994.
14. Belytschko T, Krongauz Y, Organ D, Fleming M, Krysl P. Meshless methods: an overview and recent developments. *Computer Methods in Applied Mechanics and Engineering* 1996; **139**:3–47.
15. Randles PW, Libersky LD. Smoothed particle hydrodynamics: some recent improvements and applications. *Computer Methods in Applied Mechanics and Engineering* 1996; **139**:375–408.
16. Vignjevic R, Campbell J, Libersky LA. Treatment of zero energy modes in the smoothed particle hydrodynamics method. *Computer Methods in Applied Mechanics and Engineering* 2000; **184**(1):67–85.
17. Krongauz Y, Belytschko T. Consistent pseudo derivatives in meshless methods. *Computer Methods in Applied Mechanics and Engineering* 1997; **146**:371–386.
18. Liu WK, Adee J, Jun S. Reproducing kernel particle methods for elastic and plastic problems. In *Advanced Computational Methods for Material Modeling*, Benson DJ, Asaro RA (eds), AMD, vol. 180 and PVP, vol. 33. ASME: New York, 1993; 175–190.
19. Liu WK, Jun S, Li S, Adee J, Belytschko T. Reproducing kernel particle methods for structural dynamics. *International Journal for Numerical Methods in Engineering* 1995; **38**:1655–1679.
20. Dilts GA. Moving—least squares-particle hydrodynamics I, consistency and stability. *International Journal for Numerical Methods in Engineering* 1999; **4**:1115–1155.
21. Atluri S, Zhu T. A new meshless local Petrov Galerkin (MLPG) approach in computational mechanics. *Computational Mechanics* 2000; **22**:117–127.
22. Belytschko T, Xiao S. Stability analysis of particle methods with corrected derivatives. *Computers and Mathematics with Applications* 2002; **43**(3–5):329–350.
23. Randles PW, Libersky LD, Petschek AG. On neighbors, derivatives, and viscosity in particle codes. *Proceedings of ECCM Conference*, Munich, Germany, 31 August–3 September 1999.
24. Zhang LT, Gay M. Immersed finite element method for fluid–structure interaction. *Journal of Fluids and Structures* 2007; **23**(6):836–857.

DOI: 10.1002/fld

25. Zhang L, Gerstenberg A, Wang X, Liu WK. Immersed finite element method. *Computer Methods in Applied Mechanics and Engineering* 2004; **193**:2051–2067.
26. Pita CM, Felicelli SD. Applications of the immersed element-free Galerkin method. In *Mecánica Computacional*, Cardona A, Storti M, Zuppa C (eds), vol. 27. AMCA (Asociación Argentina de Mecánica Computacional), 2008; 541–561.
27. Lancaster P, Salkauskas K. Surfaces generated by moving least squares methods. *Mathematics of Computation* 1981; **37**(155):141–158.
28. Felicelli SD, Heinrichi JC, Poirier DR. Numerical models for dendritic solidification of binary alloys. *Numerical Heat Transfer B* 1993; **23**:461–481.
29. Levin D. The approximation power of moving least squares. *Mathematics of Computation* 1998; **67**(224): 1517–1531.
30. Dolbow J, Belytschko T. An introduction to programming the meshless element free Galerkin method. *Archives of Computational Methods in Engineering—State of the Art Reviews* 1998; **5**(3):207–241.
31. Campbell J. *Castings*. Elsevier: Oxford, 2003.
32. Hypermesh 8.0, Altair Computing Inc., 1994.

DOI: 10.1002/fld